MIT Libraries | DSpace@MIT

MIT Open Access Articles

# *Time-lapse full-waveform inversion with ocean-bottom-cable data: Application on Valhall field*

The MIT Faculty has made this article openly available. ***Please share*** how this access benefits you. Your story matters.

**Citation:** Yang, Di, Faqi Liu, Scott Morton, Alison Malcolm, and Michael Fehler. "Time-Lapse Full-Waveform Inversion with Ocean-Bottom-Cable Data: Application on Valhall Field." Geophysics 81, no. 4 (June 10, 2016): R225–R235.

**As Published:** http://dx.doi.org/10.1190/GEO2015-0345.1

**Publisher:** Society of Exploration Geophysicists

**Persistent URL:** http://hdl.handle.net/1721.1/103586

**Version:** Final published version: final published article, as it appeared in a journal, conference proceedings, or other formally published context

**Terms of Use:** Article is made available in accordance with the publisher's policy and may be subject to US copyright law. Please refer to the publisher's site for terms of use.

Massachusetts Institute of Technology

GEOPHYSICS, VOL. 81, NO. 4 (JULY-AUGUST 2016); P. R225–R235, 11 FIGS.
10.1190/GEO2015-0345.1

Downloaded 07/11/16 to 18.51.1.88. Redistribution subject to SEG license or copyright; see Terms of Use at http://library.seg.org/

# Time-lapse full-waveform inversion with ocean-bottom-cable data: Application on Valhall field

Di Yang[1], Faqi Liu[2], Scott Morton[2], Alison Malcolm[3], and Michael Fehler[4]

## ABSTRACT

Knowledge of changes in reservoir properties resulting from extracting hydrocarbons or injecting fluid is critical to future production planning. Full-waveform inversion (FWI) of time-lapse seismic data provides a quantitative approach to characterize the changes by taking the difference of the inverted baseline and monitor models. The baseline and monitor data sets can be inverted either independently or jointly. Time-lapse seismic data collected by ocean-bottom cables (OBCs) in the Valhall field in the North Sea are suitable for such time-lapse FWI practice because the acquisitions are of a long offset, and the surveys are well-repeated. We have applied independent and joint FWI schemes to two time-lapse Valhall OBC data sets, which were acquired 28 months apart. The joint FWI scheme is double-difference waveform inversion (DDWI), which inverts differenced data (the monitor survey subtracted by the baseline survey) for model changes. We have found that DDWI gave a cleaner and more easily interpreted image of the reservoir changes compared with that obtained with the independent FWI schemes. A synthetic example is used to demonstrate the advantage of DDWI in mitigating spurious estimates of property changes and to provide cross validations for the Valhall data results.

## INTRODUCTION

Time-lapse seismic monitoring is widely used in reservoir management in the oil industry to obtain information about reservoir changes caused by fluid injection and subsequent production. The seismic responses change according to the fluid saturation and pressure variations in the reservoir. The optimal goal of time-lapse seismic is to track fluid flow in areas without well logs (Lumley, 2001). Conventional analysis of time-lapse seismic data gives either qualitative dynamic information, such as seismic amplitude, or indirect kinematic parameters, such as image shifts and traveltime differences. This information needs to be transferred to reservoir properties by reservoir modeling (Lumley and Behrens, 1998). Quantitative 4D techniques are used to estimate reservoir compaction and velocity changes using time shift and time strain in the data (Landrø and Stammeijer, 2004; Zadeh et al., 2011). Amplitude variation with offset (AVO) analysis inverts partial-angle stacks for elastic impedance changes (Sarkar et al., 2003; Tatanova and Hatchell, 2012). However, these methods assume simple subsurface structures, and often involve manual interpretation.

Full-waveform inversion (FWI) has the potential to estimate density and elastic parameters quantitatively (Tarantola, 1984; Mora, 1987; Virieux and Operto, 2009). Subsurface properties are updated iteratively by fitting data with modeled waveforms, which are generated by solving wave equations. Ideally, by subtracting the models inverted from each data set in a series of time-lapse surveys, the geophysical property changes over time can be quantified. Instead of analyzing small and large offsets separately as in Zadeh et al. (2011), FWI naturally takes all types of waves into account, including diving waves, supercritical reflections, and multiscattered waves. The structural depth and velocity changes can be well-represented in FWI inverted models; therefore, separate analyses are not necessary, as in conventional time-lapse methods (Landrø and Stammeijer, 2004). In addition, FWI makes no assumption about the subsurface structures and involves less manual interaction. However, FWI at the current stage still needs a fairly good starting model. Many ongoing studies focus on how to relax this

Manuscript received by the Editor 26 June 2015; revised manuscript received 7 February 2016; published online 10 June 2016.
[1]Formerly Massachusetts Institute of Technology, Earth Resources Lab, Cambridge, Massachusetts, USA; presently ExxonMobil Upstream Research Company, Spring, Texas, USA. E-mail: diyang.mit@gmail.com.
[2]Hess Corporation, Houston, Texas, USA.
[3]Formerly Massachusetts Institute of Technology, Earth Resources Lab, Cambridge, Massachusetts, USA; presently Memorial University of Newfoundland, Department of Earth Sciences, St. John's, Newfoundland, Canada. E-mail: amalcom@mun.ca.
[4]Massachusetts Institute of Technology, Earth Resources Lab, Cambridge, Massachusetts, USA. E-mail: fehler@mit.edu.
© 2016 Society of Exploration Geophysicists. All rights reserved.

Downloaded 07/11/16 to 18.51.1.88. Redistribution subject to SEG license or copyright; see Terms of Use at http://library.seg.org/

constraint (AlTheyab and Schuster, 2015; Luo and Wu, 2015; Warner and Guasch, 2015).

The most straightforward strategy of time-lapse FWI is to perform two independent inversions on each data set starting from the same initial model. The subtraction between models would give time-lapse model differences assuming the two inversions converge to a similar level in a similar number of iterations (Zheng et al., 2011; Routh et al., 2012). However, the convergence levels of waveform inversions for individual data sets are affected by data quality and computational parameters used in the inversion, which may differ between surveys. Model differences caused by different local minima between inversions may generate misleading time-lapse images. One way to mitigate the undesired deviation between models is to use the final model inverted from the base data set as the initial model for the monitor inversion. As discussed in Routh et al. (2012), most parts of the models are already close and the inversion mainly focuses on the time-lapse difference. However, this is only true when the baseline FWI is so complete that no extra updates would be generated through more iterations (Yang et al., 2015). In practice, we cannot afford an infinite number of iterations, and so the residuals due to the truncation might leak to the monitor inversion and mix with the real time-lapse difference. Watanabe et al. (2005) apply a differential waveform tomography in the frequency domain for crosswell time-lapse data during gas production and show that the results are more accurate for estimating velocity changes in small regions than those obtained using the conventional method. Onishi et al. (2009) apply a similar strategy to conduct differential traveltime tomography using crosswell surveys. Denli and Huang (2009) develop a double-difference waveform inversion (DDWI) algorithm using time-lapse reflection data in the time domain and demonstrate, using synthetic data, that the method has the potential to produce reliable estimates of reservoir changes. Similar approaches are also reported by Zhang and Huang (2013) and Zheng et al. (2011). Several publications have compared the performance of the three different strategies with synthetic examples. Raknes and Arntsen (2014) improve the convergence using a local regularization term in all three schemes and apply them on a limited-offset data set. Maharramov and Biondi (2014) compare the three schemes using frequency-domain solvers with synthetic examples and also propose using regularization to improve the results. Asnaashari et al. (2015) conduct a similar comparison study using synthetics and show that the prior model information makes the target-oriented time-lapse inversion more robust with the presence of strong noise. Nonetheless, to our best knowledge, very few large field data applications of DDWI have been reported.

A major obstruction to successful field data applications of FWI and DDWI is data acquisition. To recover a model having a broad wavenumber spectrum, low-frequency and long-offset data are required, but they are often not available in legacy seismic experiments. Advanced technologies, such as wide-aperture and wide-azimuth acquisitions, make FWI more feasible nowadays. However, DDWI requires prestack data subtractions, which impose a higher standard on time-lapse survey repeatability. One way to obtain such data is with 4D ocean-bottom cable (OBC) acquisitions using receiver cables installed on the seafloor. Source and receiver positioning discrepancies between surveys are significantly reduced compared with streamer acquisitions. The signal quality is also improved because of better receiver coupling. The repeatability of 4D OBC acquisitions appears promising for DDWI application.

Since 1998, OBC data have been collected in the Valhall field in the North Sea (Hall et al., 2005). A permanent OBC system was installed in 2003 to enable frequently repeated time-lapse surveys to help manage the field. Due to the wide aperture and high quality of the surveys, numerous studies on 2D and 3D FWI use Valhall data (e.g., Sirgue et al., 2009; Prieux et al., 2011, 2013; Liu et al., 2013; Schiemenz and Igel, 2013). Barkved et al. (2010) discuss the potential business impact of FWI and time-lapse FWI on Valhall, but technical details and comparisons between time-lapse FWI approaches were not presented.

In this paper, we first introduce three time-lapse inversion schemes: (1) using the same initial model for baseline and time-lapse inversions; (2) using the final model from a baseline inversion as the starting model for time-lapse inversion; and (3) DDWI, which uses the data difference to invert for model changes, starting from the final baseline inversion model. A 2D synthetic example using the Marmousi model is used to demonstrate how DDWI can improve the inversion quality by suppressing spurious model perturbations. We then apply all three schemes to two Valhall data sets collected 28 months apart, one as a baseline and the other as monitor. We compare the results obtained from all schemes, and we show that DDWI produces a cleaner and more interpretable image of the reservoir changes. The mechanism causing the differences between the results of different inversion schemes is discussed for the synthetic and real data. Cross validations between synthetic studies and the Valhall application enhance the credibility of the DDWI result.

## THEORY

The FWI for individual surveys minimizes a cost function of the difference between the modeled data $u$ and the observed data $d$

$$E(m) = \frac{1}{2}|d - u(m)|^2, \tag{1}$$

where $m$ is the model parameter (e.g., density, P-, and S-wave velocities) to be recovered. Gradient-based methods, such as nonlinear conjugate gradient and the Gauss-Newton method have been adopted in many studies to solve this optimization problem efficiently (Mora, 1989; Pratt et al., 1998; Virieux and Operto, 2009).

The most straightforward manner for time-lapse FWI is to repeat this process on each individual data set. One can choose the same starting model for each of the individual inversions. For example, a smooth velocity model derived from tomography or an intermediate velocity model after a few iterations of baseline FWI can be used for the inversions of the baseline and monitor data sets. The differences between the final models are considered as time-lapse changes. We label this scheme I. It is also reasonable to choose the final model of the baseline inversion as the starting model for inverting monitor data sets to achieve faster convergence. The differences between the final monitor model and the starting monitor model (which is also the final baseline model) are considered as time-lapse changes. This is labeled scheme II. We remark here that schemes I and II are using conventional FWI, while the only difference is the starting model for the monitor inversion.

Other than applying conventional FWI, the data sets can be inverted jointly. An efficient way to do a joint inversion is to apply DDWI. Similar to scheme II described above, DDWI starts from a model obtained from the baseline inversion. To include both data sets, the cost function is modified to

$$E(m) = \frac{1}{2}|(d_{\text{monitor}} - d_{\text{baseline}}) - (u_{\text{monitor}}(m) - u_{\text{baseline}}(m_0))|^2, \tag{2}$$

where $d_{\text{monitor}}$ and $d_{\text{baseline}}$ are the monitor and baseline data, respectively, and $u_{\text{monitor}}$ is the synthetic data calculated from the model $m$ that is updated in every iteration. We denote by $u_{\text{baseline}}$, the synthetic data calculated from the DDWI starting model $m_0$, which is the final model from the baseline inversion. Because $m_0$ is not updated in DDWI, $u_{\text{baseline}}$ does not change throughout the inversion process. Equation 2 can be rewritten as

$$E(m) = \frac{1}{2}|u_{\text{monitor}} - d_{\text{syn}}|^2, \tag{3}$$

where $d_{\text{syn}} = u_{\text{baseline}} + (d_{\text{monitor}} - d_{\text{baseline}})$. DDWI looks for the changes in the model that can explain the waveform changes between time-lapse data sets. It reduces the effects of uncertainties in the baseline model. The mechanism and implementation of the method are well-explained by Zhang and Huang (2013) and Yang et al. (2015).

From a computational point of view, scheme I seems to be the most expensive method because it is twice as costly as a regular FWI. Scheme II starts from a much closer model, and so requires a smaller number of iterations to converge. The cost of DDWI is similar to that of scheme II because of the closer starting point. The only extra step is to prepare the data $d_{\text{syn}}$, which includes one batch of forward simulations using the final FWI model from the baseline inversion and data subtraction.

## EXAMPLE USING SYNTHETIC DATA

In this section, we use the Marmousi model to illustrate the different behaviors of the inversion schemes introduced above and to provide context for interpreting our real data results in later sections. Figure 1a shows the true baseline P-wave velocity model. In the time-lapse velocity model, a thin layer of P-wave velocity increase is placed in the second anticline under the salt layers (bright wedges) to simulate a hardening reservoir as shown in Figure 1b. The maximum magnitude of velocity change is 200 m/s. We use five shots, marked by white stars in Figure 1a, on the water surface and 400 receivers evenly spaced at the water bottom to cover the entire area. The same source and receiver geometry is used for baseline and monitor surveys to mimic a time-lapse OBC acquisition. Synthetic baseline and monitor data are generated with a finite-difference acoustic-wave equation solver. The source time function is a standard Ricker wavelet centered at 6 Hz.

We use a Gaussian window (radius of 600 m) to blur the Marmousi model (Figure 2a) to obtain a smoothed version as the starting model for the baseline inversion. A time-domain FWI solver is adopted, and the true source function is used as the input wavelet to invert for all available frequencies (2–10 Hz) at once. The raw shot gathers are used with all offsets and wave events included (i.e., no data windowing). The conjugate gradient method is used to invert for the P-wave velocity model. After 90 iterations, we obtain the recovered baseline model shown in Figure 2b. It is slightly blurred compared with the true model due to the limited resolution of the data, but the long-wavelength components are fairly accurate. The dominant features of the structures are well-recovered, whereas some of the deeper layers underneath the salt are less resolved because of lower energy penetration.

Following scheme I, we can invert the monitor data set using the same initial model (Figure 2a) for the same number of iterations. Figure 3a shows the model difference between these final time-lapse and baseline models. The reservoir change is recovered to some extent; however, model differences also exist almost everywhere outside of the reservoir layer. Some of the false changes (e.g., in the salt layers) are as strong as the real changes. The nonlinear behavior of the inversion makes it difficult to avoid such false differences between two inversions. The model subtraction is not able to differentiate between the differences caused by time-lapse effects and the differences caused by these false changes.

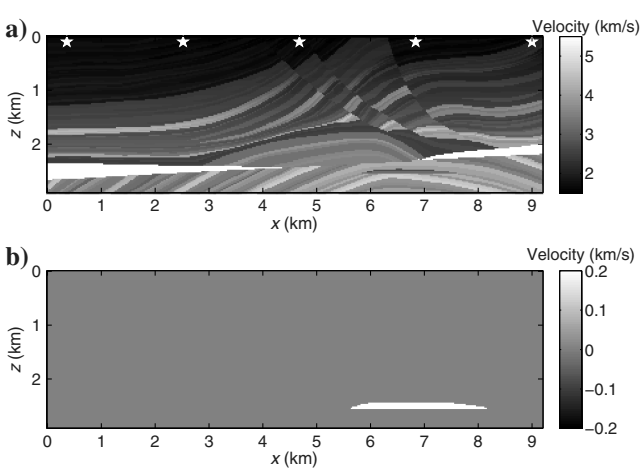


Figure 1. (a) True P-wave velocity baseline model. The reservoir is located in the anticline below the salt layers (white wedges) that have the highest velocities. Five stars mark the source locations that are used in the baseline and monitor acquisitions. (b) True time-lapse P-wave velocity changes. The layer is located in the reservoir and has a uniform velocity increase of 200 m/s, simulating a hardening effect when the reservoir is compacting.

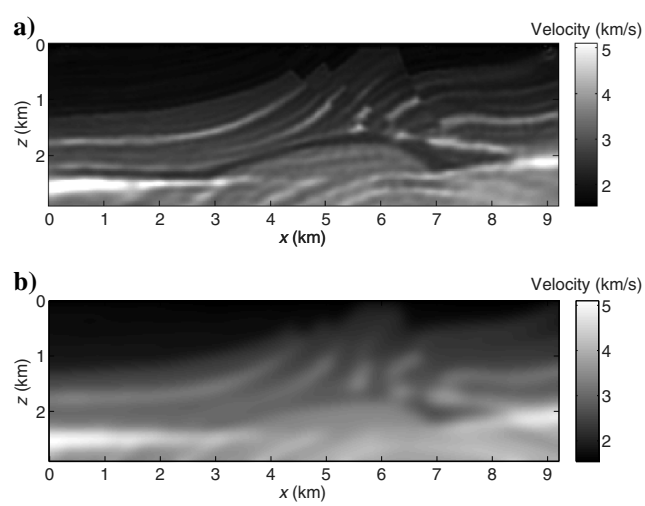


Figure 2. (a) The starting velocity model for FWI. The model is obtained by smoothing the true velocity model with a Gaussian window. (b) The velocity model obtained after 90 iterations of FWI. Details of the layers are significantly improved. The color scales in both figures are the same.

Downloaded 07/11/16 to 18.51.1.88. Redistribution subject to SEG license or copyright; see Terms of Use at http://library.seg.org/

Downloaded 07/11/16 to 18.51.1.88. Redistribution subject to SEG license or copyright; see Terms of Use at http://library.seg.org/

We can also choose to invert the monitor data set starting from the recovered baseline model (Figure 2b) as described in scheme II. Figure 3b shows the model difference between the final time-lapse and the baseline models of Figure 2b. The nonreservoir related differences are stronger than those in Figure 3a because effectively more iterations are applied to update these parameters. Therefore, parameters that are less well-estimated in the previous baseline inversion would exhibit larger magnitudes in the model difference. This explains why the real changes in the reservoir layer are saturated by the strong updates nearby in Figure 3b.

Starting from the same baseline model of Figure 2b, DDWI (scheme III) is applied to find the time-lapse changes. Figure 3c shows the time-lapse changes recovered by subtracting the baseline model from this final time-lapse model. The image is almost free of contamination. The clearest feature is the velocity increase within the reservoir layer. The shape and magnitude of the velocity changes are well-recovered. Neither the coherent structures in the shallow part nor the salt layers have any footprint in the image. This is because, as we stated in the "Theory" section, DDWI only finds the velocity perturbations that caused the data differences. Therefore, the parameters that are not completely recovered from the baseline inversion are not updated at all in DDWI.

Comparing the three images in Figure 3, it is easier to make an interpretation with the DDWI result. Without the interference from background structures, tracking the locations of changes is easier. In addition, because the magnitude of the changes is more accurately recovered, the reservoir properties inferred from this information are more reliable.

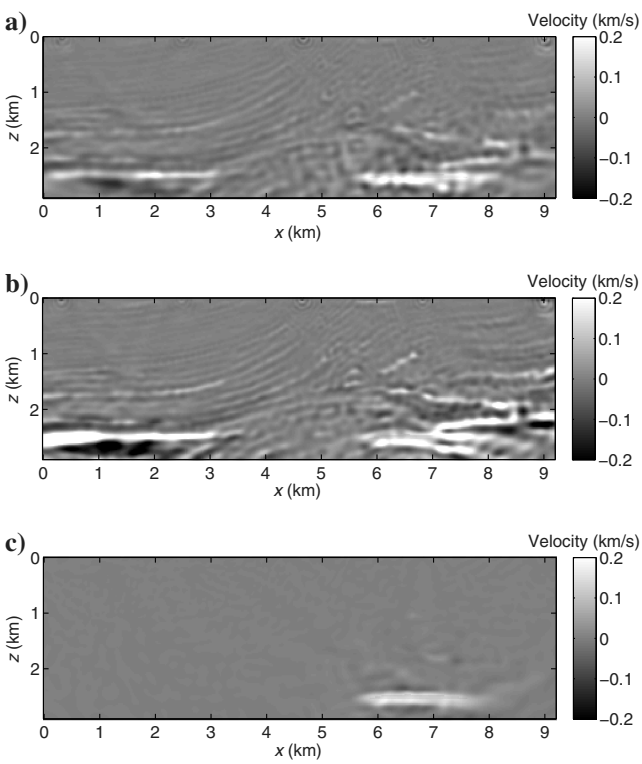


Figure 3. Time-lapse velocity changes recovered by schemes (a) I, (b) II, and (c) III (DDWI). The differences are obtained by subtracting the final baseline inversion models from the final time-lapse inversion models for each scheme. The final baseline inversion models are the same model that is recovered by the baseline inversion. Panels (a) and (b) contain strong artifacts, whereas panel (c) is clean and localized.

It is the imperfect nature of inversion that causes the difference between these methods. Even though the initial model we used here is not too far from the true model, the parameter estimation would still not be 100% accurate. The model differences between individual inversions come from the partially, but not equally, recovered parameters. Scheme I does not force the consistency of these partially estimated parameters, whereas scheme II lumps the time-lapse effects and the extra baseline updates together. DDWI removes such ambiguity by only inverting the data differences and leaving the imperfectly estimated parameters as it is. Generalizing the interpretation of these acoustic, constant density results to the viscoelastic field data case are discussed further in the "Discussion" section.

## TIME-LAPSE FWI ON VALHALL

The Valhall field sits in the southern part of the Norwegian North Sea and has been producing hydrocarbons since 1982. Recently, approved plans could potentially extend its life to 2048 (van Gestel et al., 2008). The reservoir layer is at a depth of approximately 2400 m, and its thickness ranges from 10 to 70 m. The reservoir formation consists primarily of high porosity and low permeability Cretaceous chalk. Pressure depletion of the highly porous rocks leads to significant reservoir compaction, which drives the production and induces the subsidence of the overburden structures (Barkved and Kristiansen, 2005). Significant 4D seismic time shifts due to reservoir compaction have been observed in a previous study by crossmatching of 3D streamer data collected in 1992 and 3D OBC data collected in 1998 (Hall et al., 2005). Acoustic impedance changes that reflect the depletion of the reservoir have been derived from amplitude differences by comparing marine streamer surveys in 2002 and 1992 (Barkved and Kristiansen, 2005).

To allow for more detailed and frequent analyses of induced 4D seismic changes, a permanent array, life of field seismic (LoFS), was installed in 2003 (Barkved and Kristiansen, 2005; van Gestel et al., 2008). The 4D images produced with the LoFS data provide a structural framework for identifying undrained areas, managing existing wells, and analyzing geohazard potentials (Røste al., 2007; van Gestel et al., 2008). Integrated with reservoir modeling, LoFS system reduces the uncertainties in reservoir performance predictions (van Gestel et al., 2011). We expect the constraints on the reservoir model to be improved by extracting quantitative 4D changes from the LoFS data with time-lapse FWI (Barkved et al., 2010). Because FWI includes information on structure and properties from all the data in the surveys, individual analyses on overburden changes, reservoir compaction, and reservoir property changes are naturally integrated in time-lapse FWI.

### Acquisition, repeatability, and preprocessing

As shown in Figure 4, an area of $15 \times 8$ km is densely covered by 50,000 shots (white points) on a $50 \times 50$ m grid. The missing shots in the middle of the acquisition are due to the center platform. Approximately 2400 receivers are placed a meter into the seafloor comprising 39 $km^2$ of coverage. The distance between the receivers along the cable is 50 m, and the distance between the cables is 300 m. To reduce the computation in our FWI practice, only one of every five receivers is used (spacing of 250 m along the ca-

Downloaded 07/11/16 to 18.51.1.88. Redistribution subject to SEG license or copyright; see Terms of Use at http://library.seg.org/

ble). Only the receivers that are used in both surveys are kept in our computation; in the end, 380 receivers are used in FWI (blue dots in Figure 4). The seismic experiment is repeated approximately every six months. The pressure and displacements are recorded, but only the pressure data are used in our inversion. The data sets used in this study are LoFS 10 and LoFS 12, which are 28 months apart.

Minimum preprocessing including denoising and low-pass filtering up to 7 Hz was applied to the raw shot gathers before input to FWI. No crossmatching was applied between surveys. The diving waves and reflections were kept in the shot gathers; i.e., no mute was applied. The positions of the receivers are unchanged between surveys except several cables were offline in LoFS 12. Shot positioning is very accurate in both surveys. Here, we use the distance from the actual shot location to its predesigned position as a measure of the positioning error. The error distributions are very similar between LoFS 10 and LoFS 12; 50% of the shots have errors less than 1.5 m, and 90% are less than 4 m. Because the data residual needs to be injected on regular grids in finite-difference modeling, we adopt the method of Hicks (2002) to interpolate and resample the LoFS 10 and LoFS 12 surveys to the same regular grids.

To demonstrate the excellent survey repeatability, we show example trace pairs in Figure 5. Both pairs are from the same common receiver gather. Traces in Figure 5a are from the same near-offset shot. Not only do the early arrivals fit each other well, but the coda waves are also very similar. Traces in Figure 5b are from the same far-offset shot. Despite having traveled for more than 10 km in offset, the early arrivals are still very close in phase and amplitude.

## Inversion setup

In this study, the software we use is implemented in the time domain. As a result, CPU runtime is linearly dependent on the number of sources simulated in each iteration. Therefore, reciprocity is applied to use receiver gathers as FWI input instead of shot gathers.

A few assumptions are made in the process. First, only the pressure data are used, and the acoustic-wave equation is solved to simulate the wavefield. The acoustic modeling would take care of the P-wave traveltime and the amplitudes of the near reflection angles. The P-wave AVO effect caused by the S-wave velocities would not be properly handled. However, it would not be a significant issue because for the baseline FWI, we mainly use the P-wave phase information to build the model, and no class IIp type of AVO (polarity change) is observed in the data. For the time-lapse inversion, we do not expect a strong rock matrix change within 28 months when the field was under water flooding operation. The dominant effect is fluid saturation, which would not be reflected by S-wave velocity changes. Second, only the isotropic P-wave velocity is used in the inversion. The density model is derived from the Gardner et al. (1974) equation with the updated velocity model in each iteration. It is very difficult to separate the density and $V_P$ effects on P-wave amplitudes completely. As long as the amplitude information is somewhat used, the inversion is effectively inverting for acoustic impedances. Regarding time lapse, if a $V_P$ anomaly and a density anomaly are present at the same time, it is very difficult to separate them due to their similar scattering pattern within limited offsets. Whether using the Gardener equation or doing a separate density inversion, one would not be inverting for the real density rather than

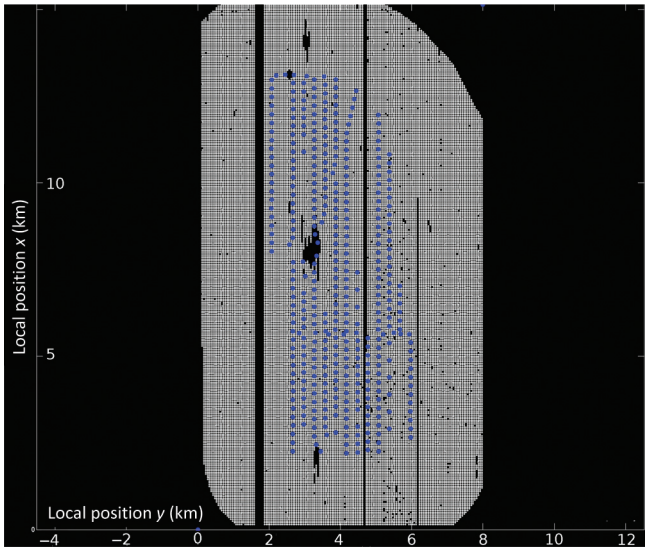


Figure 4. Layout of the LoFS survey. The white points denote the positions of shots used in the acquisitions in LoFS10 and LoFS12. The blue dots denote the positions of every five receivers. The missing shot lines are those with low quality in either survey. The irregular holes in the shot map are the locations of the platforms.

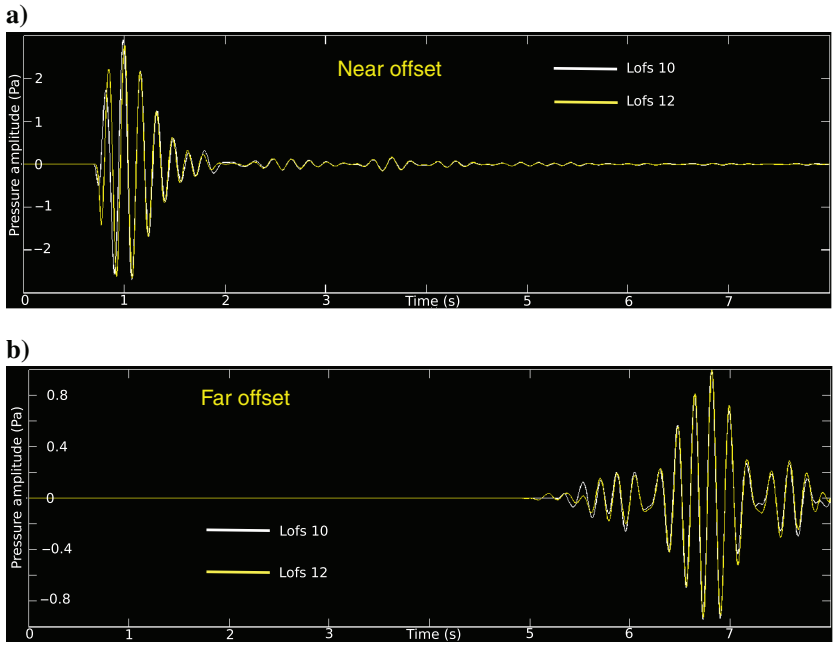


Figure 5. Traces from LoFS 10 (white line) and LoFS 12 (yellow line) are plotted together to show their similarity. All traces are from the same receiver. The pair from a near-offset shot is plotted in panel (a), and the pair from a far-offset shot is plotted in panel (b). The strong phases like the diving waves and direct waves, and the coda waves match well between surveys.

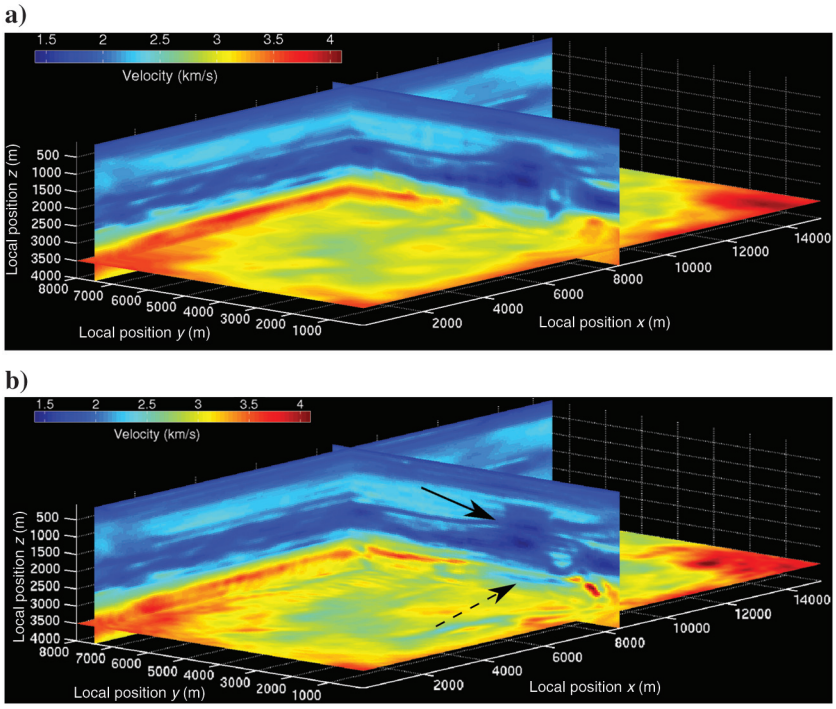


Figure 6. (a) Initial model for baseline FWI obtained by smoothing the model built by Liu et al. (2012) using a combination of FWI and tomography. (b) Baseline model obtained after 200 iterations starting from panel (a). The shallow structures are improved with higher resolution. The solid black arrow points to the gas cloud area. The low-velocity layer (pointed by the dashed black arrow) beneath the gas cloud, that is not visible in the starting model, is recovered.

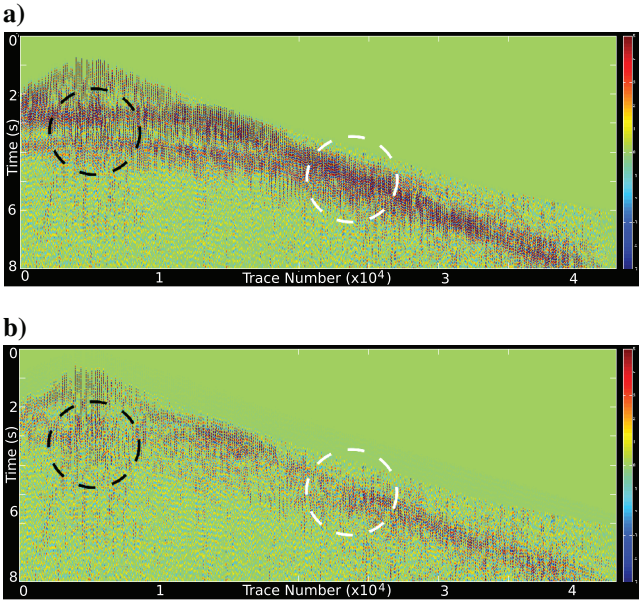


Figure 7. Data residuals of one receiver gather (a) before the baseline inversion and (b) after the baseline inversion are shown on the same color scale to show the convergence of FWI. The traces are ordered by the shot index. Residuals in far-offset diving waves (marked by the dashed white circles) and near-offset reflected waves (marked by the dashed black circles) are reduced significantly.

using it as an amplitude absorber. Third, attenuation is not included in the modeling. Instead, a trace-by-trace energy scaling strategy is used to mitigate amplitude differences (Liu et al., 2012). The impact of the energy scaling on our 4D inversion is very limited because the 4D signals are generally weak and would not contribute much to the trace energy.

The data frequencies we used range from 3 to 7 Hz. The maximum update in depth is approximately 4 km. We extracted the source wavelet from a raw near-offset trace. Because it is recorded on the seafloor, the first event is a mixture of source side ghosts, direct waves, and water bottom reflections. An effective wavelet is derived after the removal of multiples and ghosts and the application of a low-pass filter. Its quality is confirmed by carefully comparing a synthetic shot gather with the recorded data before FWI (Liu et al., 2012). A free-surface boundary condition is used to correctly model the free-surface-related multiples and the ghost effect.

## Initial velocity model

It is difficult in practice to use only FWI to invert for a good quality model starting from a poor initial guess. Several studies about FWI applications on Valhall use tomographic models as initial models (Sirgue et al., 2009; Prieux et al., 2011, 2013; Liu et al., 2013; Schiemenz and Igel, 2013). Because this study focuses on the time-lapse application, it is not necessary to start from a very simple model. Liu et al. (2012) present a Valhall velocity model using FWI combined with ray-based tomography. The final model was quality controlled by the data fit and the common image gather flatness especially for the layers under the gas cloud. Here, we use a smoothed version of that model as shown in Figure 6a, to avoid the elaborate process of initial model building. The smoothing process removed most of the structures in the model, but we left the kinematics accurate enough to avoid cycle skipping. Details about how we handle the initial model building and obtain the model in Figure 6a can be found in Liu et al. (2012, 2013).

## Baseline inversion result

We run acoustic FWI for the baseline survey data (LoFS 10) starting from the model in Figure 6a. A frequency continuation strategy is used to invert the data from 3 to 7 Hz by filtering the source wavelet and the data with a low-pass filter. The source is not reestimated at each iteration. All data are used at once without time windowing and offset muting. After 200 iterations, the baseline inversion is considered converged because the cost function has been significantly reduced; the resulting model is shown in Figure 6b. The geologic structures are recovered with high resolution. The image of the gas cloud (marked by the black arrow in $x$-$z$ slice in Figure 6b) is much improved. The thin layer under the gas cloud (pointed by the dashed black arrow) that is not visible in the starting model is resolved remarkably well. The differences between the field data and the synthetics before and after the inversion are shown in Figure 7

Downloaded 07/11/16 to 18.51.1.88. Redistribution subject to SEG license or copyright; see Terms of Use at http://library.seg.org/

for one common receiver gather. The residuals of the long-offset diving waves (white circle) and the near-offset reflections (black circle) are greatly minimized by FWI.

## Time-lapse inversion result

As in the synthetic examples, three schemes are applied to the time-lapse data set (LoFS 12). For scheme I, we start from the smooth model in Figure 6a and run the same number of iterations to invert LoFS 12 data for the time-lapse model. We choose the number of iterations as the stopping criteria because there is no absolute convergence for the real data inversion, and we can only afford a finite-compute time. Stopping at the same cost function value does not make sense because the two inversions have different cost functions (different data sets). The P-wave velocity model difference is shown in Figure 8a. In the shallow part, the differences are relatively weak, whereas the differences in the deeper part are stronger and spread out. The changes in the middle of the model show limited conformity to the geologic structures in the baseline model. For scheme II, the model in Figure 6b is used as the starting model. Figure 8b shows the model difference. Compared with scheme I, the magnitude of the difference is generally stronger. In the shallow part (around the gas cloud) and in the deep part (below the gas cloud), we find distinct velocity changes. However, the strong amplitude does not seem to be very credible for 4D changes within 2.5 years of production. The area of changes is also much wider than normally observed. For scheme III (DDWI), starting from the model in Figure 6b, we invert the data differences (LoFS 12 minus LoFS 10) for the velocity differences. As shown in Figure 8c, the velocity changes found by DDWI are much more localized than the results from schemes I and II. More importantly, the location of the changes is right at the reservoir level.

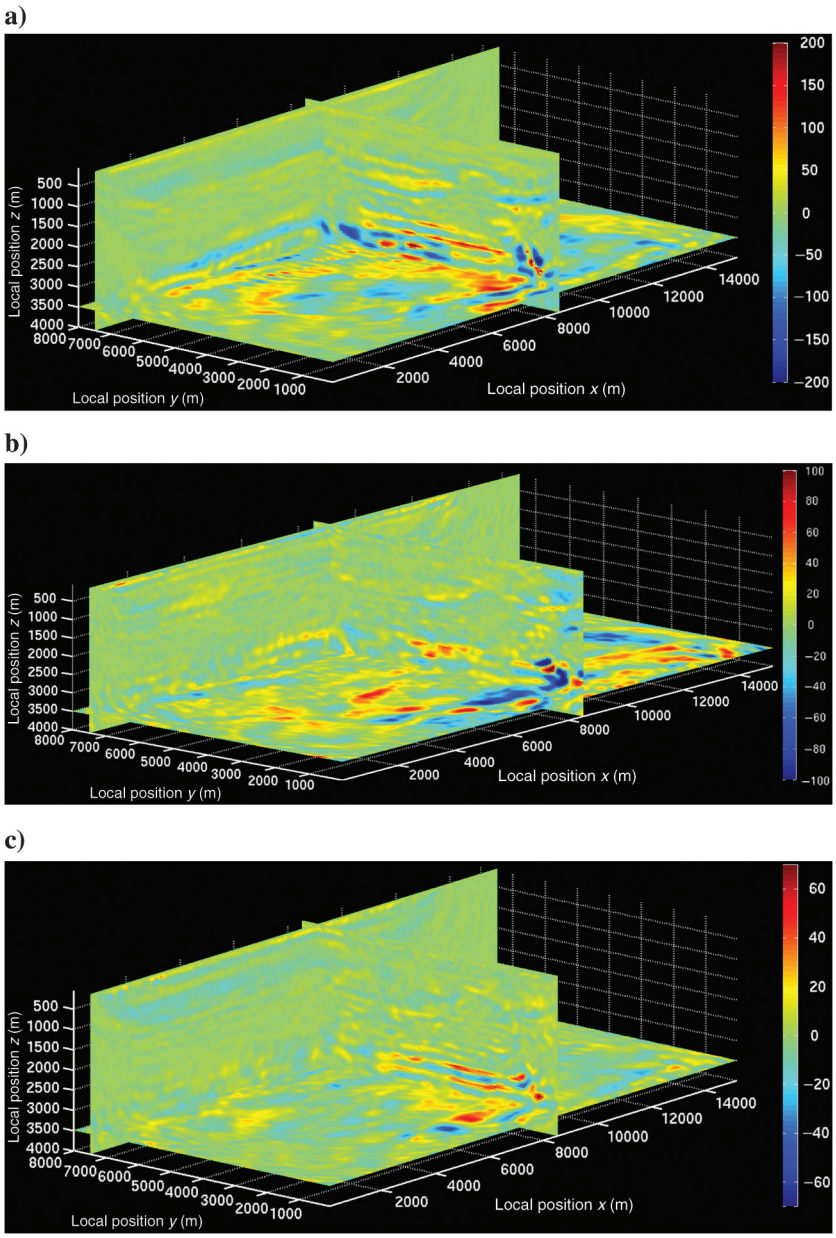


Figure 8. Three-dimensional view of time-lapse P-wave velocity changes resolved by schemes (a) I, (b) II, and (c) III (DDWI). The slices are at the same coordinates as those in Figure 6.

Downloaded 07/11/16 to 18.51.1.88. Redistribution subject to SEG license or copyright; see Terms of Use at http://library.seg.org/

Downloaded 07/11/16 to 18.51.1.88. Redistribution subject to SEG license or copyright; see Terms of Use at http://library.seg.org/

To better visualize and compare the results, we plot the 2D slices in Figures 9 and 10. Depth slices at the location of the maximum time-lapse velocity changes are shown in Figure 9. The three black squares mark the holes in the survey (Figure 4). Although there are some common features among the three images in Figure 9, the velocity changes from schemes I and II cover a much bigger area than the changes from DDWI. It is unusual to expect such broad 4D changes throughout the model. The changes in scheme I exhibit stronger amplitude to the left edge of the model, where no major production activities took place. The distribution of changes in scheme II is more consistent with the platform locations. However, it is difficult to make an interpretation from such a widespread model difference. In particular, the color scale in scheme II is two times those in schemes I and III. If shown in the same color scale, the changes in scheme II would be even broader. In contrast, the result of scheme III is confined in a reasonable area, which is also geologically meaningful.

In the cross-sectional views in Figure 10, the same velocity change volume is shown in the *x*-*z* axis. The model changes have completely different patterns. In schemes I and II, the velocity changes spread horizontally over most of the area in the deeper part of the model. Interestingly, the scheme I result shows weak changes in the production zone, but strong values on the edges. It implies that the two inversions diverged a little bit, and the model differences mainly come from the effect of different local minimum. Although the result of scheme II focuses more on the center part, the reservoir layer and the bottom of the model exhibit strong differences, which indicates that true time-lapse changes are mixed with the background model updates. In addition, some strong changes are also found in the shallow parts in schemes I and II. In contrast, in the DDWI case, the dominant change is localized in the center of the model beneath the gas cloud (dashed black circle). The changes in other parts are much weaker, and no evident changes are found in the shallow part of the model.

## DISCUSSION

The synthetic examples and the Valhall data results exhibit similar behaviors. The nonlinearity of the inversion makes scheme I generate spurious model differences. For real data, noise is different from shot to shot, and subsurface is not evenly illuminated by the acquisition. The initial model is not equally accurate for all subsurface locations. Therefore, it is more difficult to control the convergence for velocities at all positions in practice. For example, because deeper reflections have lower signal-to-noise ratio and acquisition, velocities at greater depths are less well-constrained and so differ more between independent inversions, which explains why the magnitude of changes increases with depth.

The model differences in scheme II are strongly contaminated by the extra updates to the background model (i.e., model parts without time-lapse changes) because we try to reduce the data residuals with velocity perturbations that are not related to time-lapse changes. The residuals left after the baseline inversion are much stronger than the time-lapse signals for the real data case, which explains the sig-

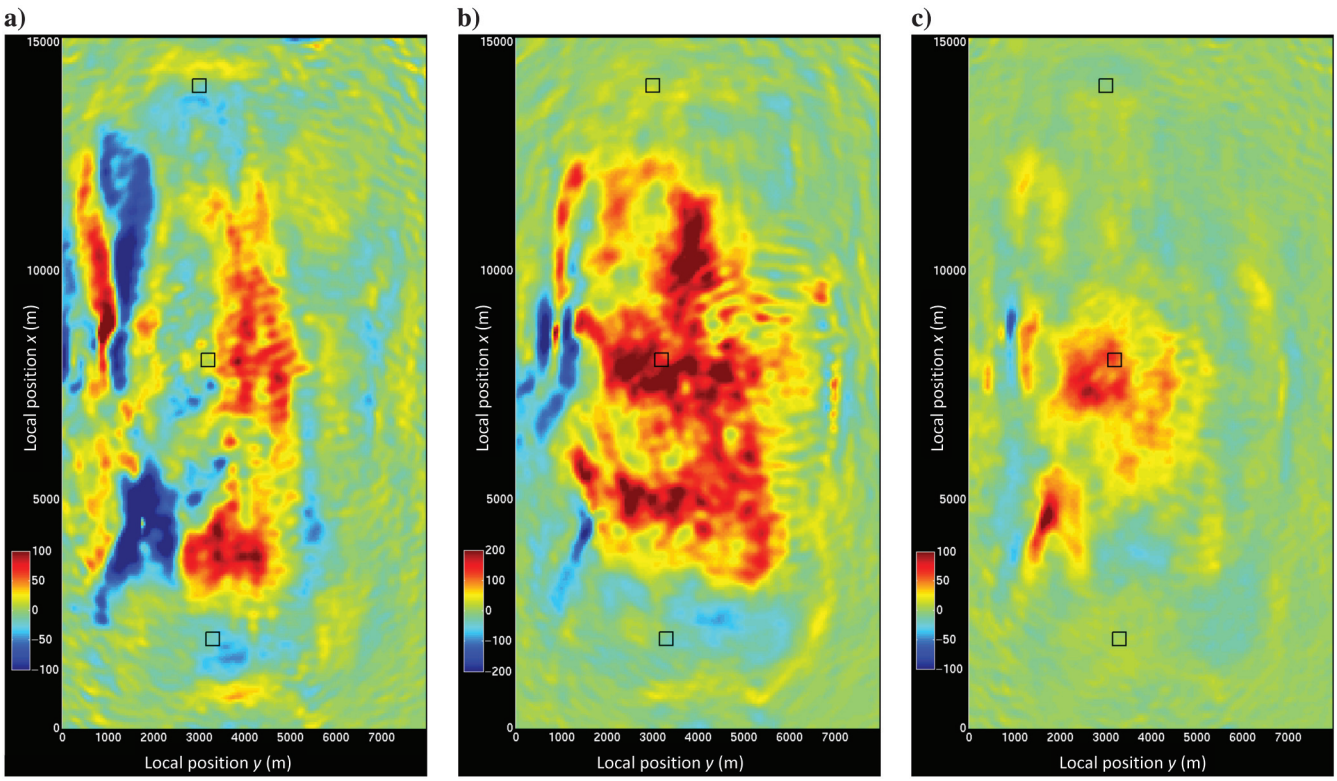


Figure 9. The *x*-*y* slice at the depth where the maximum time-lapse changes occur. Time-lapse P-wave velocity changes resolved by schemes (a) I, (b) II, and (c) III are compared. Note that the color scale in panel (b) is larger than those in panels (a) and (c) meaning stronger magnitudes. The black squares show the locations of the platforms. Note the better focusing of time-lapse changes with scheme III. The unit of the colorbar is m/s.

Downloaded 07/11/16 to 18.51.1.88. Redistribution subject to SEG license or copyright; see Terms of Use at http://library.seg.org/

nificant model differences in Figure 10b. In addition, the deeper part is less resolved than the shallow part in the baseline inversion. Consequently, we observe more updates to the deeper part in the time-lapse inversion in scheme II. One might argue that the situation would be improved by running the same number of "extra" FWI iterations on the baseline data (LoFS 10) as those run on the monitor data, and then subtracting these two models. In other words, if we run $N$ iterations to get the baseline model, and another $N$ to go from baseline to monitor, then baseline should have another $N$ iterations to equally resolve unchanging structures. In fact, this reduces to scheme I with a better starting model. We conducted this practice; however, no remarkable improvements were achieved.

The DDWI gives localized results in the synthetic and real data case studied here. Because only the velocity perturbations that can explain the data differences are used to update the model, it is easy to understand why the synthetic noise-free DDWI result in Figure 3c is so clean. One might feel uncomfortable about subtracting real data sets when there are so many uncertainties between surveys. Nonrepeatability issues, such as random noise, source wavelet discrepancy, source position error, and overburden changes, can generate significant data differences that may overwhelm the real time-lapse signals. These nonrepeatability effects are discussed and tested in detail in Yang et al. (2015), which concludes that DDWI is robust to random noise, and mild nonrepeatabilities. For the LoFS 10 and LoFS 12 surveys, the standard deviation of the source positioning error is less than 5 m. Source wavelets are well-repeated in the frequency range used in FWI, and any water velocity changes do not have a huge impact because it is a shallow water environment. Overburden changes are expected to be small because the two sur-

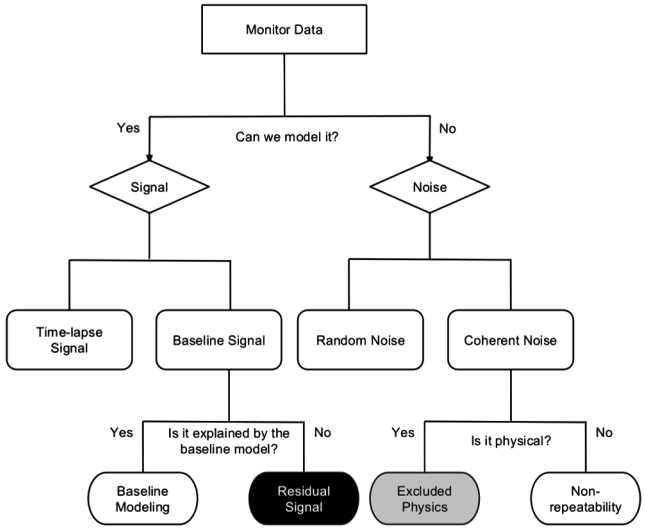


Figure 11. The decomposition of the monitor data set. The monitor data can be separated into two branches by the modeling capability. The parts that can be simulated by the modeling engine are considered as signal, whereas the rest is treated as noise. In the signal branch, part of the baseline signal cannot be explained by the current baseline model due to the imperfection of the baseline inversion. This part (the black block) would generate artificial time-lapse changes in schemes I and II, but will be canceled in DDWI. In the noise branch, these nonrepeatable components will remain in all schemes, but the repeatable components (the gray block) will be canceled in DDWI.

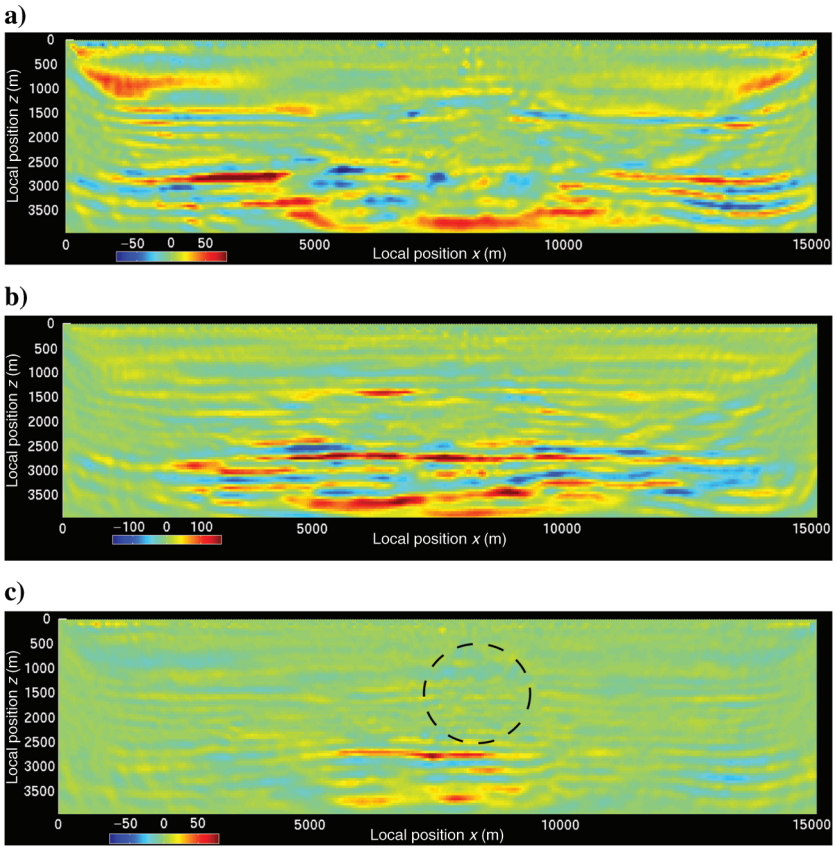


Figure 10. The $x$-$z$ slice at the location where maximum time-lapse changes occur along the $x$-axis. Time-lapse P-wave velocity changes resolved by schemes (a) I, (b) II, and (c) III are compared. (a) The scheme I result shows changes of similar magnitude at shallow and deep locations. (b) The scheme II result has fewer shallow changes but contains strong and broad changes in the deeper part. (c) The scheme III result shows localized changes in the layer underneath the gas cloud. The gas cloud region is marked with a dashed black circle. The unit of the colorbar is m/s.

Downloaded 07/11/16 to 18.51.1.88. Redistribution subject to SEG license or copyright; see Terms of Use at http://library.seg.org/

veys are only 28 months apart. All the issues are within the range where DDWI is tested to be robust.

If we take the field data results at face value, DDWI is definitely finding a time-lapse velocity change that is cleaner and easier to interpret. But to understand why this is the case, and thus to increase our confidence in our interpretation, we need to describe what we are fitting in DDWI and how this contrasts with traditional FWI. To this end, Figure 11 summarizes the various effects that we expect to see in the time-lapse data, showing those that are suppressed with DDWI as compared with standard FWI in black and gray. The data can be decomposed into two parts as shown in Figure 11: signal and noise. Within the signal branch, all the information is related to real changes in earth properties. The signal can be simulated given the true model. Due to either underfitting the data or being caught in a local minima, the inverted model can only explain part of the signal. The rest is residual signal (black in Figure 11) that we expect to cancel in DDWI and not in schemes I and II. In the noise branch, we classify noise as either coherent or random. The random component will contribute relatively little to the final image because of stacking. Coherent noise should lead to changes throughout the model, if it is constructively interfering and significant enough. Nonrepeatibilities can introduce coherent noise but are less likely to be modeled in the simulation, which is why DDWI is robust to them (Yang et al., 2015). For example, the weak variations in the shallow part of our DDWI result are likely caused by the data differences from nonrepeatibilities. These data differences are not subsurface related, but will be projected into the model. However, they could not be coherently explained by subsurface perturbations. Therefore, the resulting model changes are relatively weak. The signal that is not modeled due to incomplete physics (gray in Figure 11) in the model equations are considered as noise and has a second-order effect on the velocity change. For example, the common background anisotropy and attenuation effects are subtracted out in DDWI, and those induced by reservoir changes are relatively weak and localized. Because the model change in the DDWI example is clean and localized, it is credible that the recovered velocity change is actually the reservoir change rather than simply the movement into a different local minimum of the objective function, or simply the change one might expect if the inversion were to be continued to additional iterations.

## CONCLUSION

Advanced acquisition technologies such as OBC provide the opportunity to use high-resolution imaging methods to monitor subsurface changes. We applied DDWI on two time-lapse data sets from the Valhall field, and resolved cleaner and more interpretable time-lapse velocity changes compared with those from independent inversion schemes. The results are supported by previous studies and the synthetic tests included in this work. The nonrepeatabilities of the two surveys are mild and allow DDWI to invert for credible time-lapse P-wave velocity changes.

## ACKNOWLEDGMENTS

This work was supported by the MIT Earth Resources Laboratory Founding Members Consortium and Hess Corporation. We thank the partners of the Valhall field (BP Norge and Hess Norge) for use of the LoFS data and for permission to publish the results in this paper. We also thank M. Warner from Imperial College for providing the original FWI code.

## REFERENCES

AlTheyab, A., and G. T. Schuster, 2015, Inverting reflections using full-waveform inversion with inaccurate starting models: 85th Annual International Meeting, SEG, Expanded Abstracts, 1148–1153.

Asnaashari, A., R. Brossier, S. Garambois, F. Audebert, P. Thore, and J. Virieux, 2015, Time-lapse seismic imaging using regularized full-waveform inversion with a prior model: Which strategy?: Geophysical Prospecting, **63**, 78–98, doi: 10.1111/gpr.2015.63.issue-1.

Barkved, O., P. Heavey, J. Kommedal, J. van Gestel, R. Synnve, H. Pettersen, C. Kent, and U. Albertin, 2010, Business impact of full waveform inversion at Valhall: 80th Annual International Meeting, SEG, Expanded Abstracts, 925–929.

Barkved, O., and T. Kristiansen, 2005, Seismic time-lapse effects and stress changes: Examples from a compacting reservoir: The Leading Edge, **24**, 1244–1248, doi: 10.1190/1.2149636.

Denli, H., and L. Huang, 2009, Double-difference elastic waveform tomography in the time domain: 79th Annual International Meeting, SEG, Expanded Abstracts, 2302–2306.

Gardner, G., L. Gardner, and A. Gregory, 1974, Formation velocity and density — The diagnostic basics for stratigraphic traps: Geophysics, **39**, 770–780, doi: 10.1190/1.1440465.

Hall, S., C. MacBeth, O. Barkved, and P. Wild, 2005, Cross-matching with interpreted warping of 3D streamer and 3D ocean-bottom-cable data at Valhall for time-lapse assessment: Geophysical Prospecting, **53**, 283–297, doi: 10.1111/gpr.2005.53.issue-2.

Hicks, G. J., 2002, Arbitrary source and receiver positioning in finite-difference schemes using kaiser windowed sinc functions: Geophysics, **67**, 156–165, doi: 10.1190/1.1451454.

Landrø, M., and J. Stammeijer, 2004, Quantitative estimation of compaction and velocity changes using 4D impedance and traveltime changes: Geophysics, **69**, 949–957, doi: 10.1190/1.1778238.

Liu, F., L. Guasch, S. A. Morton, M. Warner, A. Umpleby, Z. Meng, S. Fairhead, and S. Checkles, 2012, 3-D time-domain full waveform inversion of a Valhall OBC dataset: 82nd Annual International Meeting, SEG, Expanded Abstracts, doi: 10.1190/segam2012-1105.1.

Liu, F., S. Morton, X. Ma, and S. Checkles, 2013, Some key factors for the successful application of full-waveform inversion: The Leading Edge, **32**, 1124–1129, doi: 10.1190/tle32091124.1.

Lumley, D., and R. Behrens, 1998, Practical issues of 4D seismic reservoir monitoring: What an engineer needs to know: SPE Reservoir Evaluation & Engineering, **1**, 528–538, doi: 10.2118/53004-PA.

Lumley, D. E., 2001, Time-lapse seismic reservoir monitoring: Geophysics, **66**, 50–53, doi: 10.1190/1.1444921.

Luo, J., and R.-S. Wu, 2015, Initial model construction for elastic full waveform inversion using envelope inversion method: 85th Annual International Meeting, SEG, Expanded Abstracts, 1420–1424.

Maharramov, M., and B. Biondi, 2014, Joint full-waveform inversion of time-lapse seismic data sets: 84th Annual International Meeting, SEG, Expanded Abstracts, 954–959.

Mora, P., 1987, Nonlinear two-dimensional elastic inversion of multioffset seismic data: Geophysics, **52**, 1211–1228, doi: 10.1190/1.1442384.

Mora, P., 1989, Inversion = migration + tomography: Parallel Computing, **1988**, 78–101.

Onishi, K., T. Ueyama, T. Matsuoka, D. Nobuoka, H. Saito, H. Azuma, and Z. Xue, 2009, Application of crosswell seismic tomography using difference analysis with data normalization to monitor $CO_2$ flooding in an aquifer: International Journal of Greenhouse Gas Control, **3**, 311–321, doi: 10.1016/j.ijggc.2008.08.003.

Pratt, R. G., C. Shin, and G. Hick, 1998, Gauss-Newton and full Newton methods in frequency-space seismic waveform inversion: Geophysical Journal International, **133**, 341–362, doi: 10.1046/j.1365-246X.1998.00498.x.

Prieux, V., R. Brossier, Y. Gholami, S. Operto, J. Virieux, O. I. Barkved, and J. H. Kommedal, 2011, On the footprint of anisotropy on isotropic full waveform inversion: The Valhall case study: Geophysical Journal International, **187**, 1495–1515, doi: 10.1111/gji.2011.187.issue-3.

Prieux, V., R. Brossier, S. Operto, and J. Virieux, 2013, Multiparameter full waveform inversion of multicomponent ocean-bottom-cable data from the Valhall field. Part 1: Imaging compressional wave speed, density and attenuation: Geophysical Journal International, **194**, 1640–1664, doi: 10.1093/gji/ggt177.

Raknes, E. B., and B. Arntsen, 2014, Time-lapse full-waveform inversion of limited-offset seismic data using a local migration regularization: Geophysics, **79**, no. 3, WA117–WA128, doi: 10.1190/geo2013-0369.1.

Røste, T., M. Landrø, and P. Hatchell, 2007, Monitoring overburden layer changes and fault movements from time-lapse seismic data on the Valhall

field: Geophysical Journal International, **170**, 1100–1118, doi: 10.1111/gji.2007.170.issue-3.
Routh, P., G. Palacharla, I. Chikichev, and S. Lazaratos, 2012, Full wavefield inversion of time-lapse data for improved imaging and reservoir characterization: 82nd Annual International Meeting, SEG, Expanded Abstracts, doi:10.1190/segam2012-1043.1.
Sarkar, S., W. P. Gouveia, and D. H. Johnston, 2003, On the inversion of time-lapse seismic data: 73rd Annual International Meeting, SEG, Expanded Abstracts, 1489–1492.
Schiemenz, A., and H. Igel, 2013, Accelerated 3-D full-waveform inversion using simultaneously encoded sources in the time domain: Application to Valhall ocean-bottom cable data: Geophysical Journal International, **195**, 1970–1988, doi: 10.1093/gji/ggt362.
Sirgue, L., O. Barkved, J. Van Gestel, O. Askim, and J. Kommedal, 2009, 3D waveform inversion on Valhall wide-azimuth OBC: 71st Annual International Conference and Exhibition, EAGE, Extended Abstracts, U038.
Tarantola, A., 1984, Inversion of seismic reflection data in the acoustic approximation: Geophysics, **49**, 1259–1266, doi: 10.1190/1.1441754.
Tatanova, M., and P. Hatchell, 2012, Time-lapse AVO on deepwater OBN seismic at the Mars field: 82nd Annual International Meeting, SEG, Expanded Abstracts, doi: 10.1190/segam2012-1259.1.
van Gestel, J.-P., K. D. Best, O. I. Barkved, and J. H. Kommedal, 2011, Integration of the life of field seismic data with the reservoir model at the Valhall field: Geophysical Prospecting, **59**, 673–681, doi: 10.1111/gpr.2011.59.issue-4.
van Gestel, J.-P., J. H. Kommedal, O. I. Barkved, I. Mundal, R. Bakke, and K. D. Best, 2008, Continuous seismic surveillance of Valhall field: The Leading Edge, **27**, 1616–1621, doi: 10.1190/1.3036964.
Virieux, J., and S. Operto, 2009, An overview of full-waveform inversion in exploration geophysics: Geophysics, **74**, no. 6, WCC1–WCC26, doi: 10.1190/1.3238367.
Warner, M., and L. Guasch, 2015, Robust adaptive waveform inversion: 85th Annual International Meeting, SEG, Expanded Abstracts, 1059–1063.
Watanabe, T., S. Shimizu, E. Asakawa, and T. Matsuoka, 2004, Differential waveform tomography for time-lapse crosswell seismic data with application to gas hydrate production monitoring: 74th Annual International Meeting, SEG, Expanded Abstracts, 2323–2326.
Yang, D., M. Meadows, P. Inderwiesen, J. Landa, A. Malcolm, and M. Fehler, 2015, Double-difference waveform inversion: Feasibility and robustness study with pressure data: Geophysics, **80**, no. 6, M129–M141, doi: 10.1190/geo2014-0489.1.
Zadeh, H., M. Landrø, and O. Barkved, 2011, Long-offset time-lapse seismic: Tested on the Valhall lofs data: Geophysics, **76**, no. 2, O1–O13, doi: 10.1190/1.3536640.
Zhang, Z., and L. Huang, 2013, Double-difference elastic-waveform inversion with prior information for time-lapse monitoring: Geophysics, **78**, no. 6, R259–R273, doi: 10.1190/geo2012-0527.1.
Zheng, Y., P. Barton, and S. Singh, 2011, Strategies for elastic full waveform inversion of timelapse ocean bottom cable (OBC) seismic data: 81st Annual International Meeting, SEG, Expanded Abstracts, 4195–4200.

Downloaded 07/11/16 to 18.51.1.88. Redistribution subject to SEG license or copyright; see Terms of Use at http://library.seg.org/